Comparison on Module Performance and Degradation Robustness of Two-, Three-, and Four-Terminal Perovskite Silicon Configurations Under Realistic Operating Conditions

Blom, Y.; Suprayogi, W.; Vogt, M.R.; Isabella, O.; Santbergen, R.

DOI
10.1002/pip.70066

Publication date
2026

Document Version
Final published version

Published in
Progress in Photovoltaics: research and applications

Progress in Photovoltaics: Research and Applications

WILEY

PROGRESS IN PHOTOVOLTAICS

SPECIAL ISSUE ARTICLE OPEN ACCESS

Comparison on Module Performance and Degradation Robustness of Two-, Three-, and Four-Terminal Perovskite Silicon Configurations Under Realistic Operating Conditions

Youri Blom | Wenang Suprayogi | Malte Ruben Vogt | Olindo Isabella | Rudi Santbergen

Delft University of Technology, Photovoltaic Materials and Devices Group, Delft, the Netherlands

Correspondence: Youri Blom and Rudi Santbergen (y.blom@tudelft.nl; r.santbergen@tudelft.nl)

Received: 8 July 2025 | **Revised:** 11 December 2025 | **Accepted:** 22 December 2025

Keywords: energy losses | energy yield modelling | perovskite/silicon cells | two-terminal/three-terminal/four-Terminal

ABSTRACT

Perovskite/silicon (PS) technology includes three main configurations: two-terminal (2T), three-terminal (3T), and four-terminal (4T). Previous studies have made various comparisons between these configurations, significantly advancing our understanding of these devices. While these studies mostly focus on simulations on cell level, we perform bandgap energy (E_g) optimization at the module level for different configurations under outdoor conditions. Using opto-electrical simulations, we predict the energy yield of each module at four geographical locations, with varying values of E_g. The optimal E_g for the 2T, 3T, and 4T modules are 1.62, 1.80, and 1.82 eV, respectively. We also perform a loss analysis to explore the differences in power losses among the configurations. These loss differences can be attributed to the configurations having different optimal E_g values (affecting the thermalization losses) or different module designs (affecting the interconnection losses). Among all losses, mismatch losses play the most critical role in optimizing the bandgap. Overall, all optimized configurations have similar energy yields (all differences within 1.5%) across all locations. Finally, we compare the robustness of the different configurations against different scenarios of perovskite degradation. Our results show that the 4T module is the least sensitive to degradation in the perovskite subcell.

1 | Introduction

Conventional crystalline silicon (c-Si) cells currently dominate the photovoltaic (PV) market, holding a 97% market share [1] and achieving a power conversion efficiency (PCE) of up to 27.3% [2], approaching their theoretical limit of 29.5% [3, 4]. To surpass this limit, perovskite/silicon (PS) tandem cells offer a promising alternative, with practical (considering reduced ion density, ideal series resistance, ideal transport layers, ideal bulk lifetime and improved optical performance [5]) and theoretical efficiency limits of 39.5% [5] and 42% [6, 7], respectively, and a demonstrated record efficiency of 35.0% [8].

This PS technology can come in three main configurations: two-terminal (2T), three-terminal (3T), and four-terminal (4T) configurations [9–12], as illustrated in Figure 1a.

In the 2T design, the perovskite top cell is monolithically stacked atop the silicon bottom cell, forming a wafer-based module (as shown in Figure 1b). The top and bottom cells are connected in series with a tunnel junction or recombination layer [9, 14], requiring current matching between top and bottom cell [12]. While this design constraint limits flexibility, the interconnection of the cells within the module remains relatively simple, as the tandem cell has the same number of terminals as a

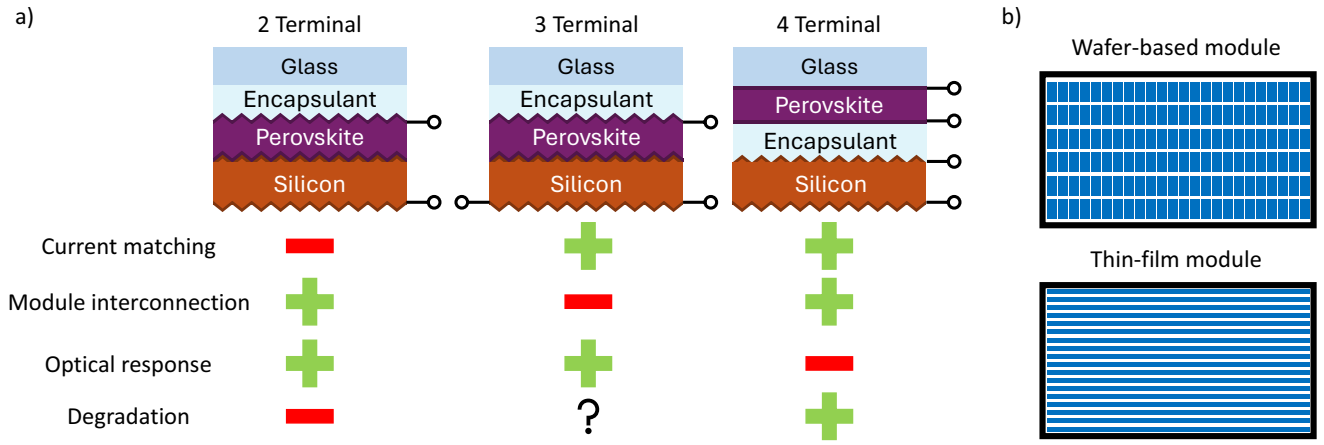

FIGURE 1 | (a) An overview of the 2T, 3T, and 4T configurations at module level and a comparison of different aspects, such as current matching, module interconnection, optical response, and robustness against degradation. (b) The difference between a wafer-based and a thin-film module. The schematics are taken from [13].

single-junction c-Si cell. Additionally, the top cell is conformal and follows the texturing of the bottom cell, enhancing the optical performance [15].

The 3T configuration introduces an additional contact, allowing independent current flow in each subcell and removing the need for current matching [16]. This additional contact can be placed between the subcells or at the rear of the bottom cell, as demonstrated by Warren et al. [17] or a heterojunction bipolar transistor (HBT) architecture can be considered [18]. This study only analyzes the option with an additional contact at the rear side. However, the 3T configuration requires more complex module interconnections, typically forming a parallel/series connection [19], and experiences end-losses [9]. The cause for the end-losses are discussed in Section 2.3. As the 3T module is a wafer-based, similar to the 2T configuration, it also has low optical losses.

In the 4T configuration, the top and bottom subcells are electrically separated, enabling each to operate at its own current. Unlike the other configurations, the perovskite layer is deposited on the glass instead of directly on the silicon cell [20], with an encapsulant layer separating the top and bottom cells. Consequently, the 4T device consists of a wafer-based submodule for the silicon cells and a thin-film submodule for the perovskite cells, as shown in Figure 1b. This electrical separation simplifies module interconnections compared to 3T, forming two distinct series-connected strings [9]. However, the 4T design can have more optical losses due to an additional layers [12], and the fact that top cell does not follow the same texturing as the bottom cell, as they are not stacked monolithically. Furthermore, 4T modules require an optical coupling layer to advance the optical absorption [21]. Additionally, it should be realized that if both submodules are not voltage matched, both strings need their own maximum power point tracking [9].

Each configuration also differs in robustness against degradation. A study by Qian et al. [22] showed that 4T modules are more resilient against perovskite degradation than 2T modules. Specifically, Qian's findings indicate that for every 1% increase in degradation rate in the perovskite layer, the efficiency must rise by 2% in 2T devices but only 1% in 4T devices to maintain performance. However, 3T modules were not considered in this comparison.

Assigning a universally superior configuration is challenging, as each offers unique advantages. Several studies have used optoelectrical simulations to quantify performance differences among these configurations. Futscher et al. [23] calculated efficiency limits for 2T, 3T, and 4T devices under standard test conditions (STC), finding maximum efficiencies of 45.1%, 45.3%, and 45.3%, respectively. These maximum efficiencies are lower in virtually all realistic outdoor conditions [7]. Their study also examined how the optimal bandgap energy (E_g) varies across configurations, identifying ideal values of 1.73 eV for the 2T and 1.81 eV for both the 3T and 4T configurations.

Additional studies provide insights into energy yield (EY) at the cell and module levels. Gota et al. [24] found that the 3T configuration has higher EY across various locations and demonstrated greater resilience to variations in perovskite thickness and E_g than the 2T design. McMahon et al. [25] showed that the 3T configuration could outperform 2T in energy production at the module level, provided that a sufficient number of cells are included, such that the end-losses are small. In an optical study, Singh et al. [26] compared the average photo-generated current for 2T, 3T, and 4T modules in operating conditions, showing how the absorbed light is affected by changes in perovskite thickness and bandgap energy. Lastly, Kikelj et al. [27] concluded that 3T devices can surpass 2T devices in performance with optimized module design.

While these studies have advanced the understanding of each configuration, certain aspects remain underexplored. Key considerations like cell-to-module losses and the optimization of E_g at the module level, accounting for realistic optical and electrical properties, have not been thoroughly addressed. These cell-to-module losses include optical losses due to glass and encapsulant, non-active area losses, and ohmic interconnection losses. Additionally, to the best of the authors' knowledge, the robustness against perovskite degradation for 3T modules has not been studied.

This study evaluates the potential of 2T, 3T, and 4T devices at the module level. Using a PS cell from the literature as a benchmark, we simulate the EY while accounting for various cell-to-module losses. The optimal E_g is determined for each configuration, and all losses are quantified to facilitate a comprehensive comparison. Finally, we simulate different degradation scenarios to assess the robustness of each configuration.

It is important to note that this study focuses solely on monofacial modules. Given that bifacial technology is expected to dominate in the future [1], including in IBC module architectures, further studies on 2T, 3T, and 4T bifacial modules can be considered in future work.

2 | Methodology

All simulations are conducted using the PVMD Toolbox [13, 28, 29], a modeling framework for calculating the energy yield of PV modules. As described in detail by Vogt et al. [28], the PVMD Toolbox consists of sequential simulation steps, each modeling a different aspect of the PV module. First, the spectral response of the encapsulated solar cell is simulated. This spectral response is then used to calculate the absorbed irradiance, also accounting for shading by other modules in the field. To calculate the absorbed irradiance, the module orientation and the geographical location should be specified. Then, the cell temperatures are calculated by considering different heat flows. Lastly, the annual energy yield is obtained by calculating the electricity production for each hour in the year based on hourly weather data and integrating over time. It is important to realize that all simulation steps are based on first-principle physics, meaning empirical fitting is only used for the modeling of meta-stability, as explained later in this section. Here, we summarize the components relevant to this study and discuss the inputs used. The design of the cells within the PV modules are based on the 32.5% efficient 2T PS cell by Mariotti et al. [30] with a perovskite bandgap energy of 1.68 eV, which has been integrated in the Toolbox in earlier work [13, 29]. This bandgap energy, however, is also an input parameter that can be varied, as also demonstrated in the earlier work.

In previous work, the PVMD Toolbox was validated for STC performance in PS tandem cells (error lower than 2% [13]) and for outdoor performance in c-Si modules (root mean square error of 4.5% [28]) At the end of this section, we will extend the validation to PS tandem cells under outdoor operation.

2.1 | Optical Modeling

Optical simulations were performed with GenPro [31], which applies the net radiation method [32]. Required inputs include the thickness (d) and complex refractive index ($N(\lambda) = n(\lambda) + j \cdot k(\lambda)$) of each layer, enabling calculation of the implied photo-current density. More details on this calculation is provided in the Supporting Information.

Figure 2 illustrates the optical structures of each configuration. The structures and reported thicknesses are based on the PS cell by Mariotti et al. [30] with some thicknesses slightly adjusted to have a good match between simulation and measurement. The bottom cell has texturing on both sides with pyramids of 5 μm. In the 3T configuration, which features both positive and negative contacts on the rear, a gapless Interdigitated Back Contact (IBC) architecture is considered. GenPro performs one-dimensional absorption simulations, so only one rear-side layer can be included. The Supporting Information shows that using either the positive or negative layer yields similar absorption profiles. For this study, we used the a-Si(p) layer in the optical simulations.

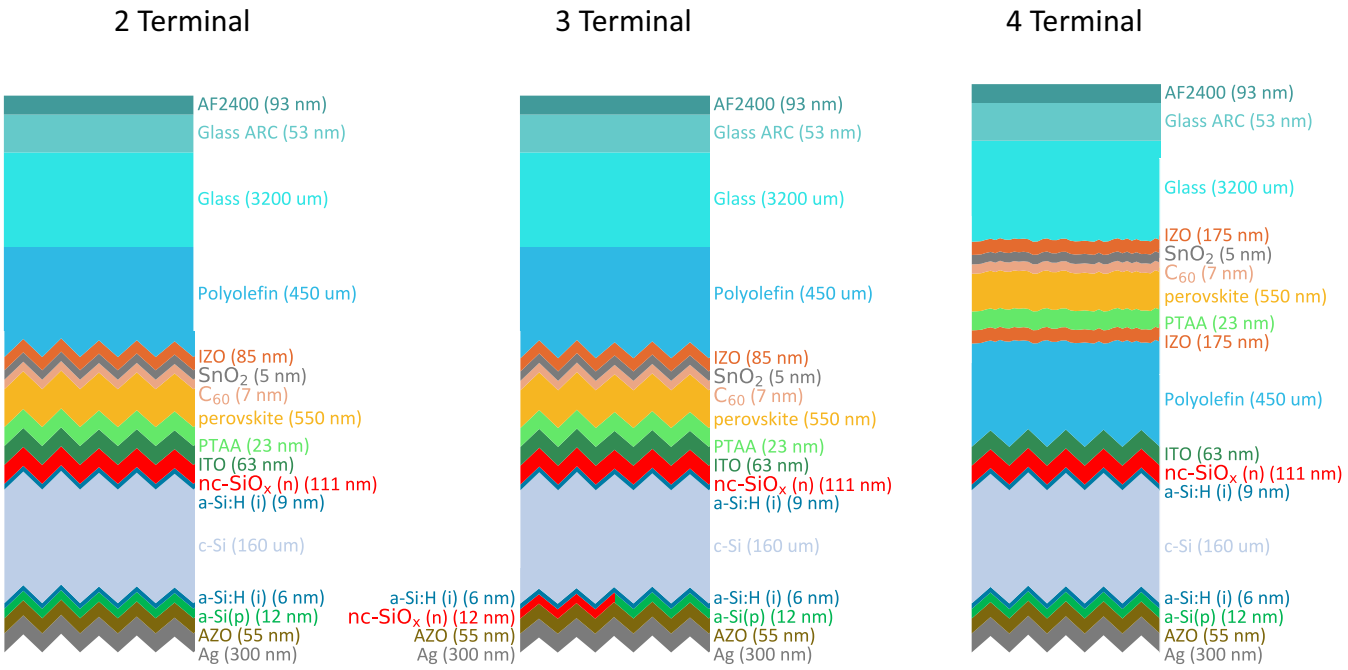

FIGURE 2 | The structures that are used as input for the optical simulations. For the 3T case, we simply consider a gapless IBC architecture.

The 2T and 3T modules uses indium zinc oxide (IZO) as transparent conductive oxide (TCO), being similar to the state-of-the-art reference solar cell by Mariotti et al. [30] The thin-film submodule in the 4T configuration, however, must provide sufficient lateral conductivity where cells are interconnected through a series of laser scribes. The monolithic patterning follows the usual P1-P2-P3 sequence: P1 opens the front electrode, P3 separates the back electrode, and P2 bridges the back electrode of one cell to the front electrode of the next through the TCO layer. Together, these scribes define the individual cells and establish the series connection within the module [33]. When connected, the current needs to be collected over the entire length of the cell, instead of only to the nearest metal finger, requiring a low resistivity for the TCO layer. Therefore, the 4T modules uses fluorine-doped tin oxide (FTO) as TCO, as it has a lower resistivity ($1.0 \cdot 10^{-4}$ Ω cm$_{-2}$ [34]) compared to IZO ($4.5 \cdot 10^{-4}$ Ω cm$_{-2}$ [35]), is therefore better suited for thin-film modules. Additionally, the TCO thickness is larger for the 4T modules, as it was found in previous work that this is beneficial for thin-film modules [13]. Furthermore, the perovskite subcell in the 4T modules is deposited on glass that has been preprocessed with Asahi U-type texturing [36].

When cells are integrated into a module, some active area is lost due to metallization (for wafer-based modules) or laser scribing (for thin-film modules). We account for this by defining a shaded-area factor (k_{shaded}) that excludes shaded areas from current generation. The output current (I_{out}) is then calculated as

$$I_{out} = (1 - k_{shaded}) \cdot A_{cell} \cdot J_{act}, \tag{1}$$

where A_{cell} is the cell area, and J_{act} is the current density of the cell's active area.

The value of k_{shaded} depends on the origin of the active area losses, and is therefore different for wafer-based and thin-film modules. For wafer-based modules, these losses come from metal fingers needed for the current collection. We assumed a metal coverage of 5%, based on the work of Rehman et al. [37]. However, the effective area that is lost can be 60% lower due to internal reflections [38], leading to a value of 2% for k_{shaded} in wafer-based modules. In thin-film modules, the laser scribing that connects the cells requires an area that cannot be used for current collection. In previous work [13], we calculated k_{shaded} to be 8%, which depends on the widths of P1, P2 and P3. Besides these non-active area losses due to metalization, there are also non-active area losses due to cell spacing. This is further discussed in Section 2.3.

2.2 | Electrical Modelling

As the details for the electrical framework have been fully explained in previous work [13, 28, 29], we only highlight the electrical structures used for the simulations. Figure 3 shows the circuit representation of each configuration. Each subcell is represented with a calibrated one-diode equivalent circuit model (including own series and parallel resistors), and resistances are added to represent the current collection losses. The explanation of how the calibrated one-diode equivalent circuit models are created and used is provided in the Supporting Information. An important assumption is that the same electrical performance of the perovskite and silicon subcells is used for all configurations. This also means that same electrical performance is considered for the 3T configuration, that employs an IBC silicon bottom cell. The reason for this assumption is that the advanced semiconductor analysis (ASA) [39], the software utilized for the semiconductor simulations, only considers one-dimension.

Since the process of current collection differs for wafer-based modules and thin-film modules, different values of resistances are used. Wafer-based modules experience ohmic losses as the current needs to be collected by metal fingers on top of the cell. This metallization is represented by a resistance ($R_{con,met}$) of 3.9 mΩ, as calculated by Jung et al. [40]. In thin-film modules, cells are connected through laser scribing, with ohmic losses occurring through the TCO layer that connect the cells. Based on the method in earlier work [13], we have calculated that these ohmic losses can be represented by a resistance ($R_{con,tf}$) of 9.7 mΩ.

2.3 | Module Interconnection

As mentioned before, the various configurations have different module interconnections. Figure 4 shows the interconnection scheme of the different configurations. The 2T and 4T follow a relative simple interconnection with, respectively, one and two series-connected strings of subcells. For the 3T module, we use the interconnection proposed by McMahon et al. [41], where m bottom cells connect in parallel with n top cells, requiring voltage matching. It can be seen that, due to this connection, m bottom cells and n top cells cannot contribute to the

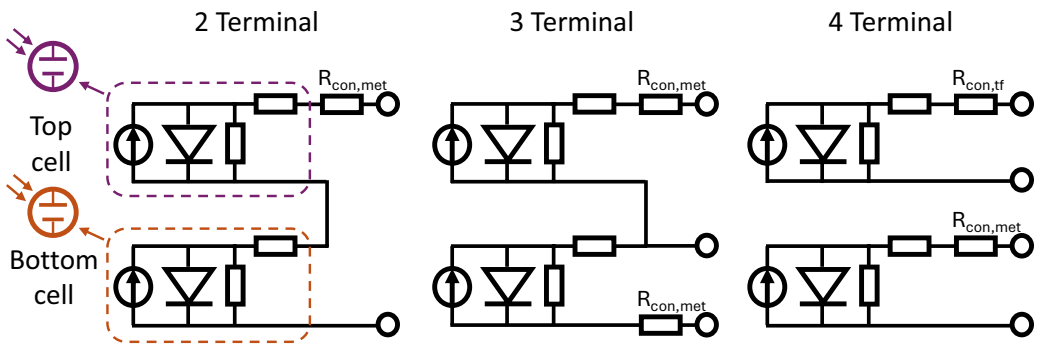

FIGURE 3 | The circuit representation of the electrical simulations.

power generation, representing the end losses. In our work, we assume $m = 2$ and $n = 1$, as shown in Figure 4, minimizing the end losses. To justify this assumption, the Supporting Information contains a bandgap optimization at STC for different values of m and n, showing that the chosen combination has the highest potential. Additionally, the Supporting Information provides full implementation details and validation with a circuit simulator.

Table 1 summarizes the module sizing for both wafer-based and thin-film modules. For wafer-based modules, we used G12 wafers with half-cut cells, anticipated to be a dominant format in the coming decade [1]. The width of thin-film cells is set at 7.5 mm, based on Castriotta et al. [33], adjusted slightly to ensure equal submodule areas. It should be realized that for both submodules A_{mod} does not equal $A_{cell} \cdot N_{cells}$, as some area is lost due to cell spacing and edge spacing. The cell spacing for wafer-based and thin-film based modules are assumed to be 0.8 and 0.0 mm. The value for thin-film modules is taken to be 0, as all non-active area due to laser-scribing is included in k_{shaded}.

An important characteristic that will be used in Section 4 are the so-called *mismatch losses*, which represent the losses when individual subcells cannot operate on their individual maximum power point. The mismatch losses are calculated according to our definition from earlier work [7] and are written as

$$P_{mism} = \sum_{i=1}^{N_{cells}} \left(P_{mpp,top-i} + P_{mpp,bot-i}\right) - I_{mod} \cdot \left(V_{mod} + I_{mod} \cdot R_{con} \cdot N_{cells}\right), \tag{2}$$

where P_{mpp,top_i} and P_{mpp,bot_i} are maximum power point of the individual top and bottom subcell, respectively, I_{mod} and V_{mod} is the module output current and voltage, respectively. By using this approach, the mismatch losses include deviations in the maximum power point voltage (V_{mpp}) and maximum power point

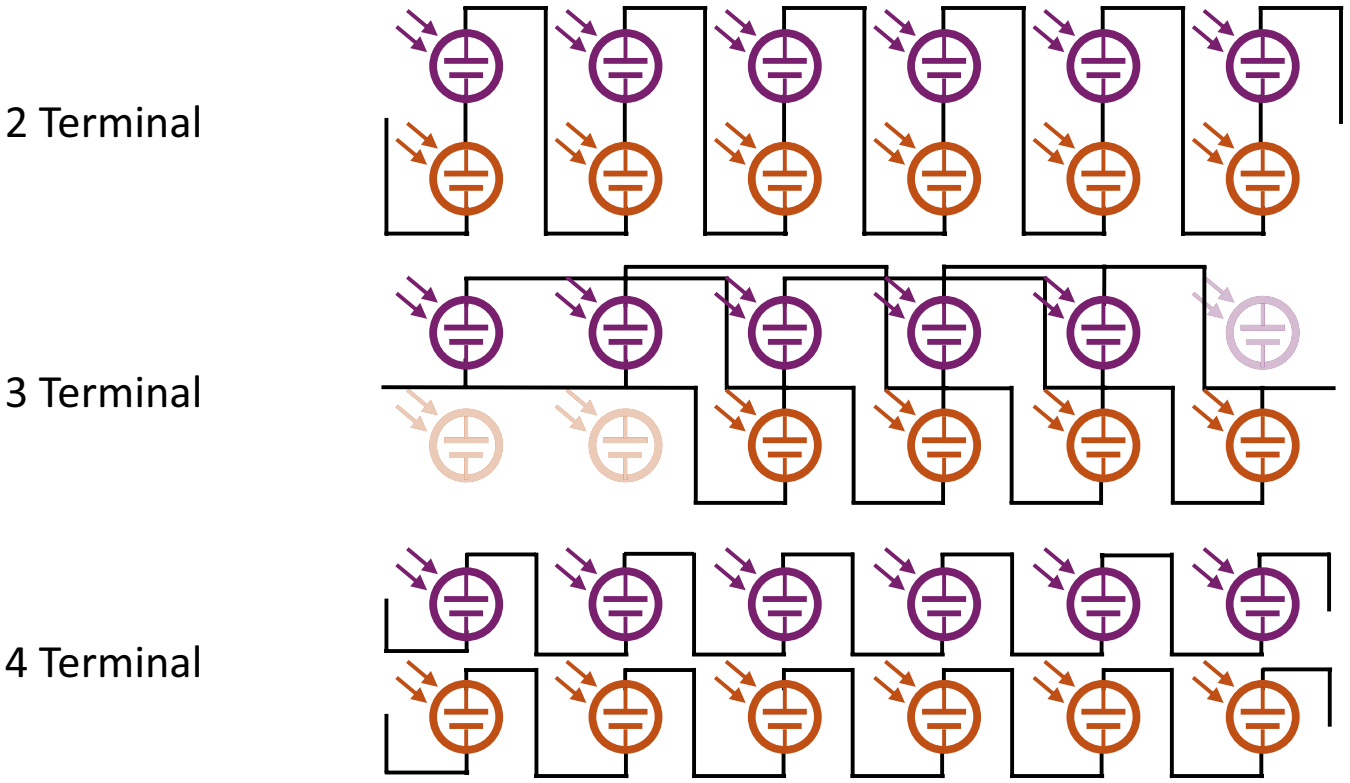

FIGURE 4 | The module interconnection of the different configurations. The blue and red diodes represent the perovskite and silicon subcells, respectively. For the 3T configuration, two bottom cells and one top cell are not connected, representing the end-losses as they cannot contribute to the power generation.

TABLE 1 | The geometry of the wafer-based and thin-film-based module.

Model type	$A_{cell}(l \times b)$ [mm2]	N_{cells} [-]	$A_{mod}(l \times b)$ [m2]	cell spacing [mm]	edge spacing [mm]
Wafer-based	210×105	144	3.285	0.8	10
Thin-film	2540×7.5	168	3.275	0.0	10

Note: The cell spacing of the thin-film modules is 0, as the dead area due to laser scribing is fully considered by k_{shaded}.

current density (J_{mpp}), but also account for the end-losses in 3T devices.

2.4 | The Modeling of Meta-Stability

Perovskite cells experience a reversible efficiency change during light and dark cycles [42, 43], known as the so called *meta-stability effect*. This phenomenon, where efficiency initially starts lower but improves with light exposure [44], has been incorporated into the PVMD Toolbox using the methodology from Remec et al. [43], which models an initial voltage loss that recovers under illumination. It should be noted that this effect is distinct from degradation, which has an irreversible effect on the efficiency. The impact of including the Light Soaking (LS) effect is discussed in the Supporting Information.

2.5 | The Simulation of Different Degradation Scenarios of Perovskite Subcells

Perovskite degradation behavior remains only partially understood, and there is insufficient long-term performance data for PS devices at the module level. Therefore, we use a similar approach as Orooji and Paetzold [45], simulating different degradation scenarios in the perovskite cell. This way the focus is not on physical processes and specific degradation mechanisms that are occurring, but rather the impact of cell level degradation on the module performance. The simulated degradation is applied to the electrical simulation of the perovskite cell, leaving the optical and electrical performance of the silicon cell unchanged.

Figure 5 illustrates the degradation scenarios considered in this work. Performance losses are modeled as reductions in short-circuit current (I_{sc}), open-circuit voltage (V_{oc}), or fill factor (FF), with degradation level (k_{deg}) representing losses specific to the perovskite top cell. I_{sc} degradation is simulated by reducing the current source, while V_{oc} degradation is achieved by increasing the diode's saturation current (I_0) in the equivalent circuit (Figure 3). FF degradation is modeled by increasing the diode's ideality factor, with I_0 adjusted to maintain consistent V_{oc}.

Figure 5 also shows the change in J_{mpp} and V_{mpp} (indicated with crosses). Whereas degradation in I_{sc} and V_{oc} only affects J_{mpp} and V_{mpp}, respectively, while keeping the other quantity constant, the degradation in FF equally affects the J_{mpp} and V_{mpp}. It should be realized that degradation in FF can also be achieved by adjusting the resistances of the equivalent circuit, potentially changing the trajectory of the MPP, and therefore, the results. In this work, we did not employ the latter approach to solely focus on the degradation of the perovskite subcells, rather than on the eventual degradation of the perovskite interconnections.

2.6 | Validation for Outdoor PS Devices

As mentioned earlier, we extend previous validations to PS tandem cells under outdoor conditions. Remec et al. at the Helmholtz-Zentrum Berlin (HZB) [43] reported data for a 24.2%-efficiency tandem PS cell operating in Berlin over 330 days. We used the PVMD Toolbox to simulate this device's performance.

It is important to note that the cell used for validation has a lower quality (24.2% STC efficiency) compared to the reference cell (32.5% STC efficiency) used in simulations. For the validation cell, an additional parallel diode was included in the electrical characterization to simulate extra losses at the interfaces, as explained in our previous work [13]. However, for the simulations, we used the higher-quality cell without the additional diode to more accurately represent the full potential of 2T, 3T, and 4T modules manufactured with state-of-the-art techniques. Additionally it should be noted that the reference cell has an area of 1 cm2, which is significantly smaller than the modules in the simulations.

Figure 6a, b, and c compare simulated and measured P_{mpp}, J_{mpp}, and V_{mpp}, respectively, for 10 selected days in the first five months of 2022. These days have been selected such that they represent

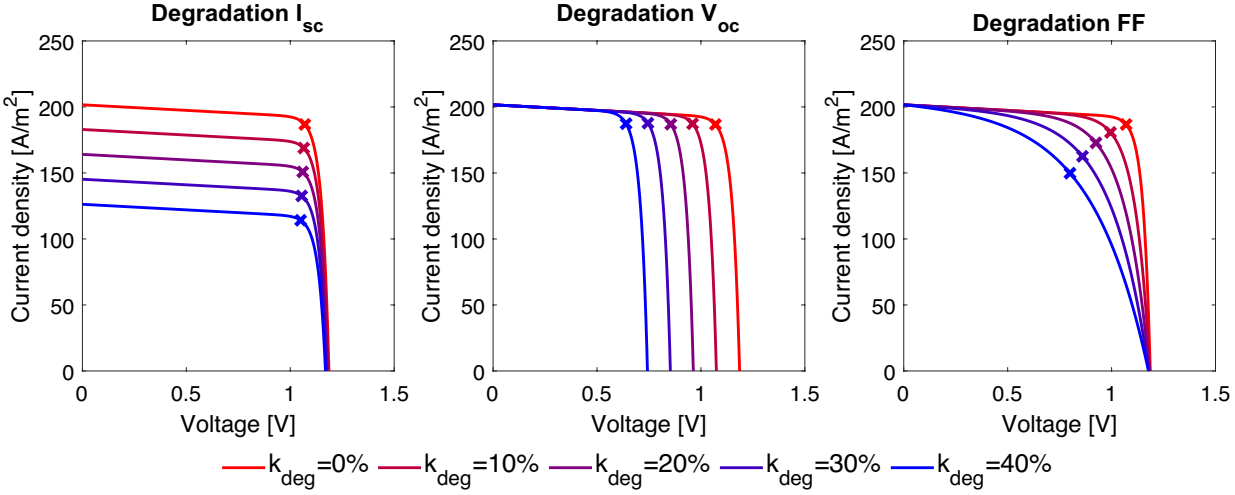

FIGURE 5 | The different degradation scenarios that are considered in this study. As example the perovskite with a E_g of 1.62 eV is shown. The maximum power point of each IV curve is indicated with a 'x'.

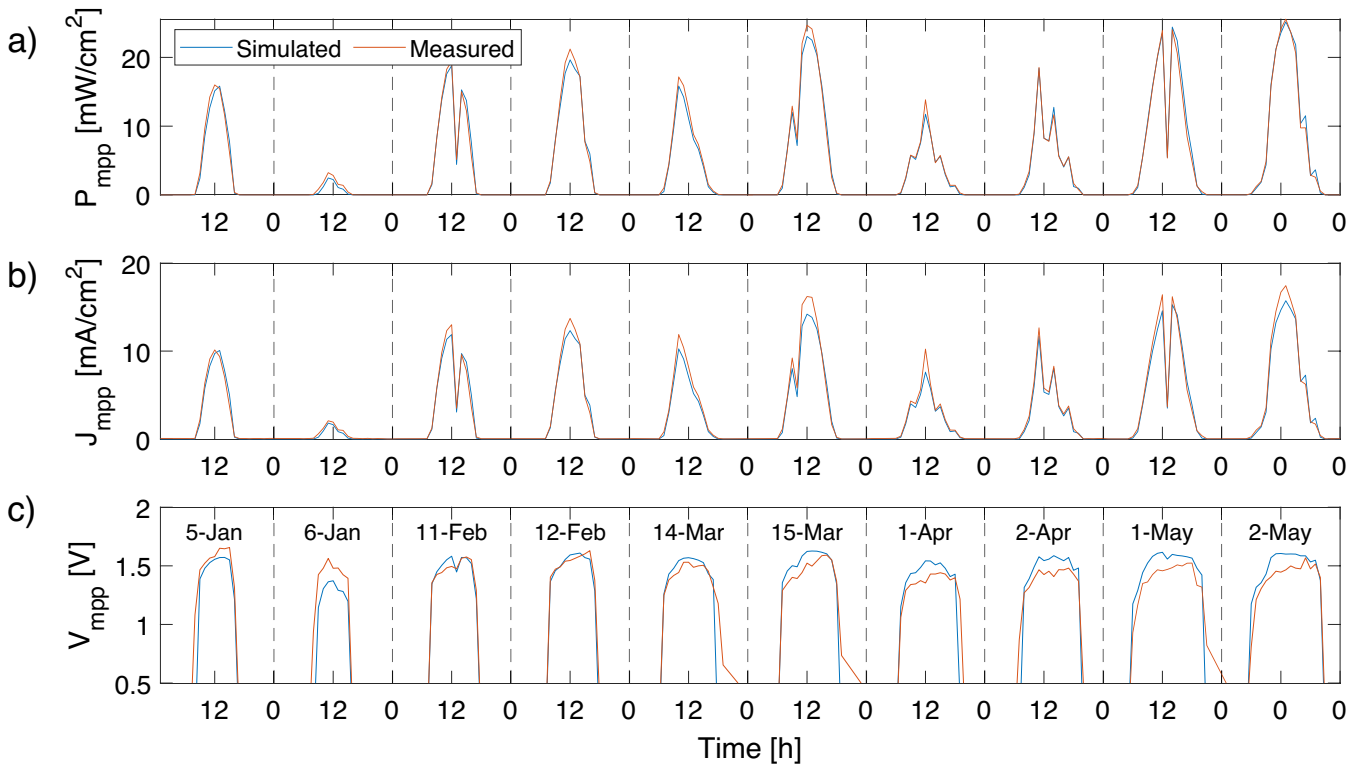

FIGURE 6 | The outdoor validation of a perovskite silicon cell in Berlin performed by HZB. a), b), and c) show the measured and simulated P_{mpp}, J_{mpp} and V_{mpp}, respectively, for 10 selected days in the first five months of the year. The RMSE between the measured and simulated output power in the first 137 days is 1.98 mW cm2, and the weighted relative error is 12.2%.

different months, have a significant amount of irradiance, and the output power have been measured correctly. While P_{mpp} and J_{mpp} align closely, there are slight discrepancies in V_{mpp}, likely due to temperature dependency differences between measurement and simulation (discussed further in the Supporting Information).

Overall, the root mean square error (RMSE) between the simulated and the measured output power of the first 137 days of the experiment is 1.98 mW cm2, and the power-weighted relative error is 12.2%. This period was selected to avoid degradation behavior observed in the tandem cells later, as it could influence the outcome of the scenario based degradation modelling of this paper by including an underlying specific degradation mode. This shows that the PVMD Toolbox can be used to accurately simulate the performance of perovskite silicon devices under outdoor conditions.

It should be realized that the validation is only performed for 2T devices. This is because, to the best of the authors knowledge, no publicly available data can be found that reports the outdoor performance of 3T and 4T devices. In future work, the validation of the PVMD Toolbox can be extended to other configurations as well.

3 | Input for Case Studies

The methodology described in the previous section is applied to determine the optimal E_g for different operating conditions. Specifically, we simulate the module performance of 2T, 3T, and 4T devices across a range of bandgap energies and geographic locations. This section explains how the bandgap variations are modeled and describes the characteristics of each location.

Another parameter that could be varied for optimization is the thickness of the perovskite layer, as it affects the current absorption in both cells. However, in previous work [13, 29] we found that the bandgap energy has a stronger impact on the energy yield than its thickness. The Supporting Information shows the energy yield of different configurations at different thicknesses, showing that the bandgap energy has a much bigger impact than the thickness. As another varying parameter would exponentially increase the number of simulations, the thickness of perovskite has been kept fixed at 550 nm, being similar to the reference cell of Mariotti et al. [30].

3.1 | Varying the Bandgap Energy

The bandgap energy significantly influences both the optical and electrical performance of a device. In the optical simulations, $N(\lambda)$ of the perovskite layer changes as a function of E_g. We use the approach from our previous work [46, 47] to predict $N(\lambda)$ for all desired bandgap energies, based on measured data from Manzoor et al. [48]. Since complete $N(\lambda)$ data for the full E_g range is unavailable, we extrapolate from Manzoor's measurements to cover our target bandgap range. This predicted $N(\lambda)$ is then used in GenPro to simulate absorption profiles for each E_g value.

In the electrical modeling, E_g serves as a direct input to generate the IV curve of the perovskite cell. Our earlier studies [13, 29] demonstrated how changes in bandgap energy affect both the optical and electrical performance of a 2T PS cell. The effect of E_g on the cell JV curve and its circuit parameters can be found in the Supporting Information.

To illustrate the effect of E_g variation on the 2T, 3T, and 4T modules, Figure 7 shows the power output at STC for each configuration across different perovskite bandgap energies. Among the three, the 2T module exhibits the highest power at STC, followed by the 3T and then the 4T configurations. The optimal E_g is lower for the 2T configuration due to its current-matching requirements, while the 3T and 4T configurations have a similar optimal E_g. A more detailed analysis of these differences is presented in the next section.

3.2 | Different Locations

To explore how optimal bandgap energy may vary across climates, we perform the bandgap optimization for several geographic locations. We selected four distinct locations, each representing a different climate type according to the Köppen-Geiger-Photovoltaics (KGPV) classification [49, 50] and a machine learning based PV climate classification (ML-PV) [51]. Table 2 provides key characteristics of these locations. For each location, we consider a fixed tilt PV system with the module tilt specified in Table 2 with an inter-row spacing of 8 meters. Additionally, we obtain the hourly data of a typical meteorological year (TMY) from Meteonorm [52].

Another characteristic of each location is the spectral irradiation and the average photon energy (APE). Figure 8 shows the annual spectral irradiance as received by the module in each location. The APE for each location is calculated by dividing the total irradiance over the total number of photons. Lagos and Shanghai have a higher APE than the other locations, implying a slight blue-shift for these locations.

4 | Results

The outlined methodology is applied to simulate the energy yield (EY) of the 2T, 3T, and 4T modules under the described operating conditions. For each location, we evaluate the module performance across various perovskite bandgap energies from 1.50 to 2.00 eV, in increments of 0.02 eV. First, we identify the optimal E_g for each condition. Then, we compare configurations in detail by quantifying the different types of losses in the PV module. Finally, we assess robustness under different degradation scenarios.

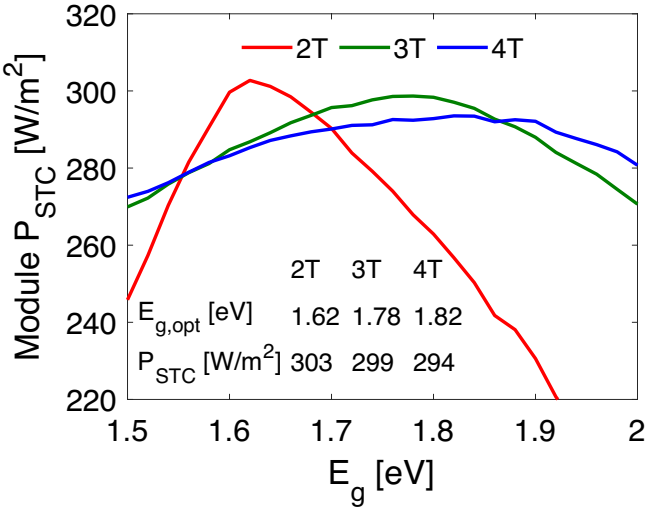

FIGURE 7 | The perovskite bandgap optimization of the different modules under STC.

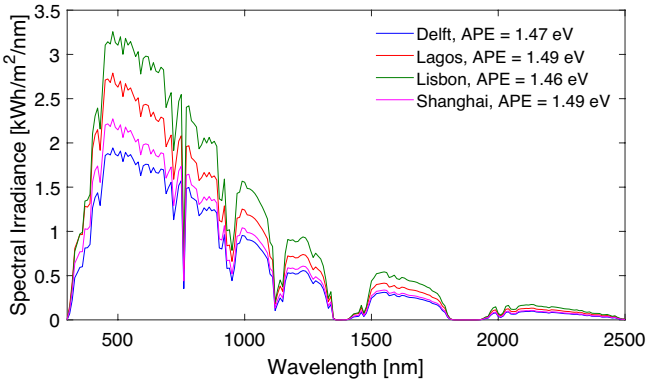

FIGURE 8 | The spectral irradiation received at each location and the corresponding APE. It can be seen that both Lagos and Shanghai have a slight blue shift compared to the other locations.

TABLE 2 | The main TMY characteristics of the selected locations.

Location	Annual global horizontal irradiation [kW h m₂]	Weighted average ambient temperature [°C]	KPGV	ML-PV	Optimal module tilt [°]
Delft	1018	16.2	DL	Tem1	31
Lagos	1642	29.4	AH	Tro2	5
Lisbon	1758	20.6	DH	Tem5	28
Shanghai	1271	21.7	DM	Tro1	17

Note: The ambient temperature is weighted with the global horizontal irradiance. This metric is chosen as, in our opinion, it better represents the operating conditions of the PV modules than the simple time average of the ambient temperature. The selected module tilts are chosen such that they maximize the annual front-side irradiation for each location in a free-horizon scenario.

4.1 | Optimal Bandgap Energy

Figure 9 presents the annual EY across different locations for each simulated bandgap energy, with dashed lines indicating the optimal E_g at STC. The 2T configuration shows the highest sensitivity to deviations from its optimal E_g because current matching is required between the top and bottom cells. In the 3T configuration, voltage matching is necessary, but this matching is less sensitive to bandgap variations, resulting in a flatter EY curve. This is shown in the Supporting Information, where the JV curve of the perovskite subcell is shown for different bandgap energies. It can be seen that the J_{sc} changes more than the V_{oc}, explaining why the 3T configuration is less sensitive to bandgap changes than the 2T configuration. Since 4T modules do not require matching between subcells, their EY curve is the flattest, showing the least sensitivity to bandgap deviations.

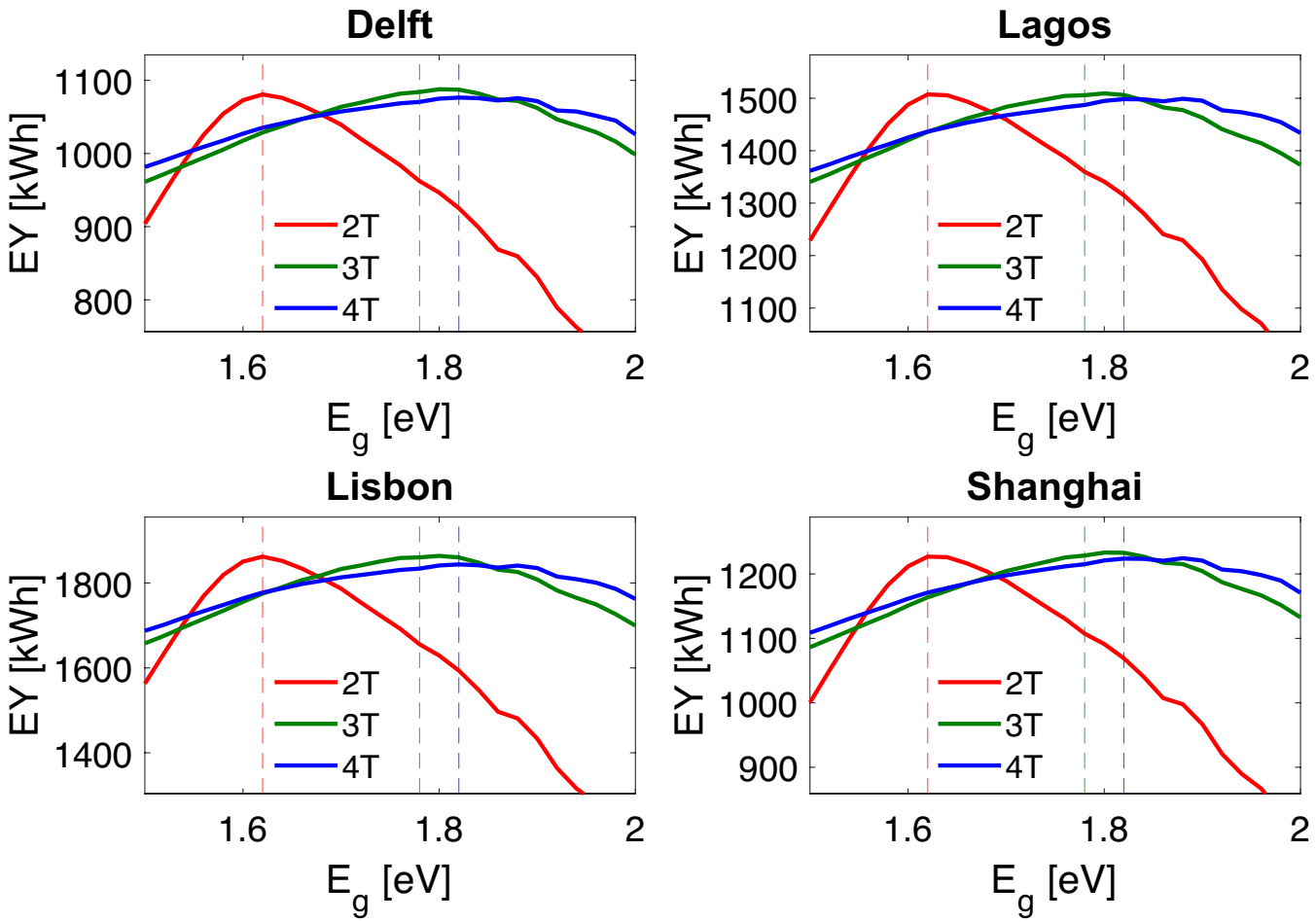

FIGURE 9 | The bandgap optimization under outdoor operating conditions for the various configurations. The dashed lines indicate the optimums at STC.

TABLE 3 | The optimal E_g and corresponding annual EY for all operating conditions, expressed in [eV].

	2T		3T		4T	
Operating conditions	E_g [eV]	EY [kWh]	E_g [eV]	EY [kWh]	E_g [eV]	EY [kWh]
STC	1.62	—	1.78	—	1.82	—
Delft	1.62	1081	1.80	1088	1.82	1076
Lagos	1.62	1507	1.80	1509	1.88	1499
Lisbon	1.62	1862	1.80	1864	1.82	1844
Shanghai	1.62	1227	1.80	1233	1.88	1225

Note: For 2T devices, the optimal bandgap is the same for all conditions, whereas the 3T configuration has a slightly lower E_g for STC. In 4T devices, the optimal bandgap fluctuates the most.

Table 3 shows the optimal E_g and corresponding EY for each scenario. The optimal bandgap at STC (as dashed lines in Figure 9) is also a good predictor for optimal E_g under outdoor conditions. For both the 2T and 3T configurations, the optimal E_g is 1.62 eV and 1.80 eV, respectively, and is consistent across locations, though the 3T device has a slightly lower optimal bandgap at STC. Only the 4T configuration shows notable variations, with an optimal E_g of 1.82 eV in STC, Delft, and Lisbon, but 1.88 eV in Lagos and Shanghai. This difference arises due to a more blue-rich irradiance spectrum in Lagos and Shanghai (as indicated in Figure 8), where a higher bandgap reduces thermalization losses. It should be realized that this apparent significant shift is mostly due to the relative flat shape of the 4T performance, meaning that there is little difference in EY between the different bandgap energies.

As shown in Figure 9 and Table 3, energy yields at the optimal E_g are similar across configurations, with all differences within 1.5%. Nonetheless, the 3T module, despite its end-losses, achieves the highest EY across all locations.

4.2 | Comparison in Losses

To better understand the difference in performance for the different configurations, we analyze the various losses that are present. Using the approach described in earlier work [7], all losses in the PV module are quantified. In this approach, 16 loss components are defined and grouped into four categories (fundamental, optical, electrical, and system losses), such that the sum of all losses and the efficiency equals 100%. Figure 10 shows the losses of the optimized PV modules in Delft. Since the losses comparison among the configurations are found to be similar for all locations, only the results of Delft are presented in the main text. The results for the other locations are reported in the Supporting Information.

It should be realized that the differences in loss distributions are caused by the configurations having different optimal bandgap energies or the configurations deploying a different module design. Figure 11 illustrates how some highlighted losses change with E_g for each configuration. The trend for all losses is provided in the Supporting Information. In some plots, not all lines are visible as their values are very similar across configurations. In case only two lines overlap, additional legends are placed to indicate which lines correspond to which configuration. This figure can be used to explain the differences observed in Figure 10. We discuss the four categories separately and explain what causes the differences among the configurations.

4.2.1 | Differences in Fundamental Losses

The fundamental losses only depend on the fundamental properties of the device, such as E_g. Therefore, these losses (as shown in Figure 11) only depend on the bandgap energy, but are similar among the configurations. The differences, visible in Figure 10, for this category are solely caused by the configurations having different bandgap energies. For example, the higher thermalization losses (19.7%) in the 2T configuration, compared to the 3T and 4T configurations (18.6%), are caused by its lower bandgap energy.

4.2.2 | Differences in Optical Losses

In contrast to the fundamental losses, differences in optical losses are mostly caused by differences in module design. As the 2T and 3T have a similar module design, these configurations have similar optical losses, while the 4T module shows higher optical losses. The higher losses for the 4T module can be attributed to greater contact shading losses (due to a larger k_{shaded} in thin-film modules), and more reflection losses, due to its less effective texture morphology and non-optimal optical coupling layer between the top and bottom subcells.

On the contrary, however, the 4T module has lower cell-spacing losses, due to the lower cell spacing in thin-film modules, and lower parasitic absorption losses. The lower parasitic absorption in 4T modules can mainly attributed to the higher reflection

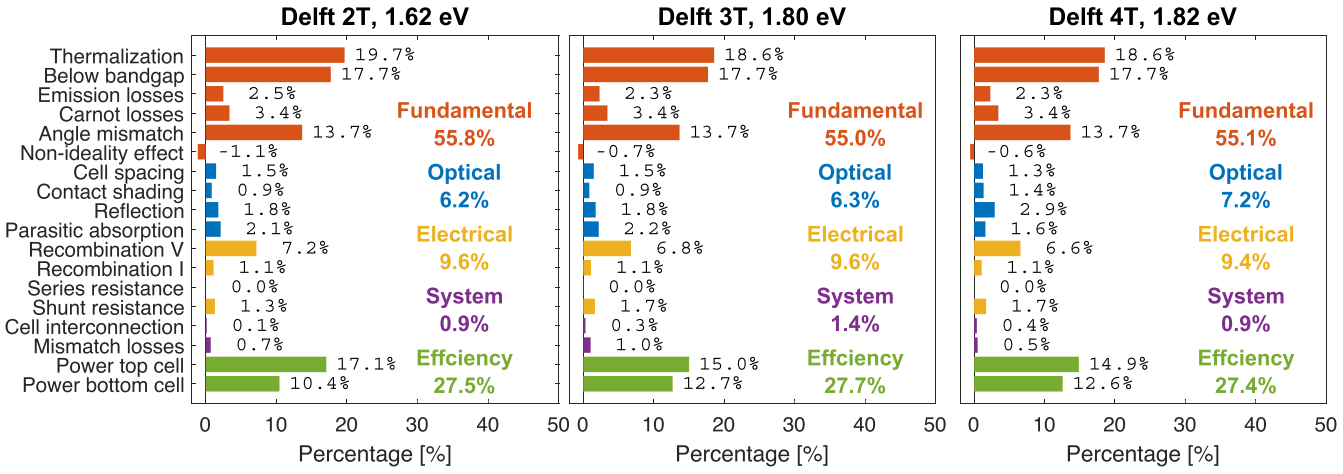

FIGURE 10 | The loss analysis for the 2T, 3T, and 4T modules operating in Delft. 16 loss components are grouped into four categories such that the sum of all losses and the efficiency equals 100%, which is equal to the in-plane irradiation on the module area.

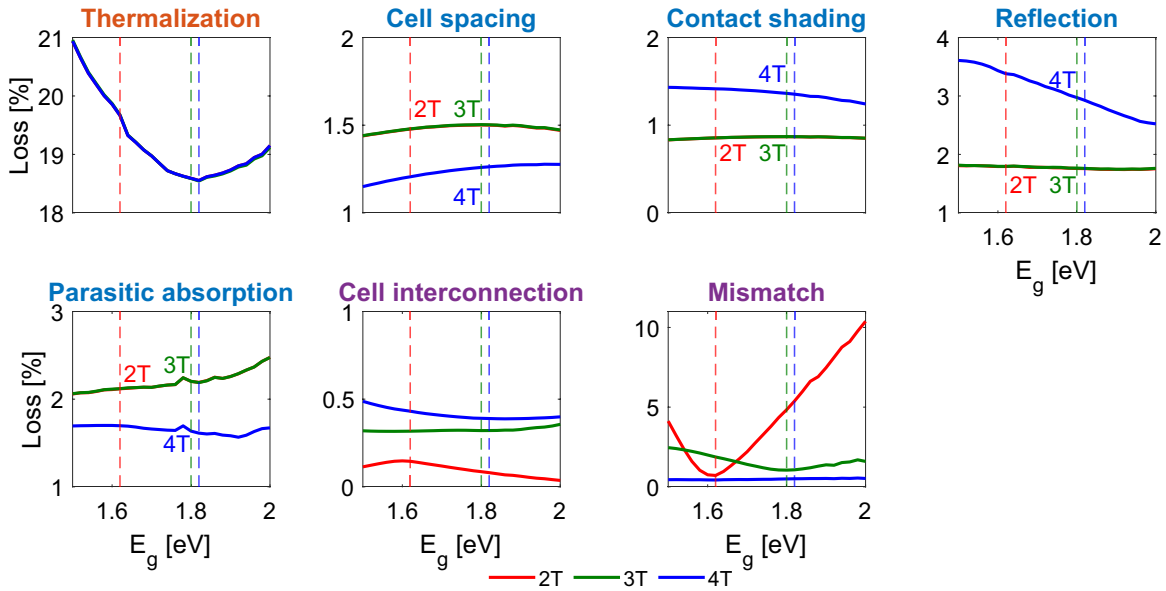

FIGURE 11 | The value for the highlighted losses at different bandgap energies for all modules located in Delft. For each configuration, the optimal bandgap energies in Delft are indicated with dotted lines. The titles in all figures indicate the losses category according to the color scheme in Figure 10. For some plots, not all configurations are visible, as the lines overlap due to similar values. In case only 2 lines overlap, additional legend are provided to identify the curves.

values, as shown by the absorption profiles which can be found in the Supporting Information.

4.2.3 | Differences in Electrical Losses

As shown in Figure 10 and Figure 11, the electrical losses are very similar for the different configurations. This is because the electrical losses account for all losses introduced by the components of the equivalent circuit, combining both recombination and resistive losses within the cell. Losses caused by differences in layer stacks and cell interconnections are instead captured by the optical and system losses, respectively. The electrical parameters are derived from the same equivalent circuit model, meaning that design variations among configurations have little impact on electrical losses. The only minor differences observed are primarily due to the modules operating at different bandgap energies.

4.2.4 | Differences in System Losses

Lastly, there are variations in the cell interconnection and mismatch losses. Interconnection losses are the highest in 4T due to $R_{con,tf}$ being larger than $R_{con,met}$. The 3T device experiences more interconnection losses than the 2T configuration due to added rear-side contact resistance.

Mismatch losses in the 2T and 3T modules significantly depend on E_g (Figure 11, bottom right), as it affects current and voltage matching, respectively, explaining why the optimal E_g closely aligns with the values that minimize mismatch losses. The 4T device, requiring no current or voltage matching, has the lowest mismatch losses. The small, but non-zero, mismatch losses are caused by the fact that the contact resistance slightly influences the operating point of the cells.

4.3 | Robustness Against Degradation

Lastly, we examine the robustness of each configuration against each degradation scenario. As mentioned before, this comparison has already been made for 2T and 4T devices in literature [22], but to the best of the authors' knowledge not for 3T devices.

For all scenario's described in Section 2.5, we rerun annual EY simulations on the optimized modules at different k_{deg} values.

Figure 12 shows the degradation impact on annual EY for the PV modules in Delft, with results for other locations available in the Supporting Information. For comparison, the energy yield of a single-junction module (Module STC efficiency of 20.4%) composed solely of silicon heterojunction (SHJ) cells is represented by a dashed line. These SHJ cells are based on the bottom cell of the considered PS tandem cell and it is assumed that they have no degradation.

In all scenarios, the energy yield of the undegraded tandem modules are approximately similar (see $k_{deg} = 0$), as the configurations have similar efficiencies in Figure 10. This similarity will remain for values of k_{deg} up to around 10%. However, these energy yields will differ for larger values of k_{deg}, depending on the type of degradation. When degradation affects I_{sc}, the 2T configuration shows the largest EY drop due to its current-matching requirement. For V_{oc} degradation, the 3T configuration is most affected, due to its voltage-matching requirement. Under *FF* degradation, the 2T and 3T configurations are similarly affected, as losses in *FF* cause both losses in J_{mpp} and V_{mpp}. Overall, the 4T configuration proves least vulnerable to perovskite cell degradation in all scenarios, as its top and bottom subcells operate independently. This independence makes the 4T module the most robust against degradation.

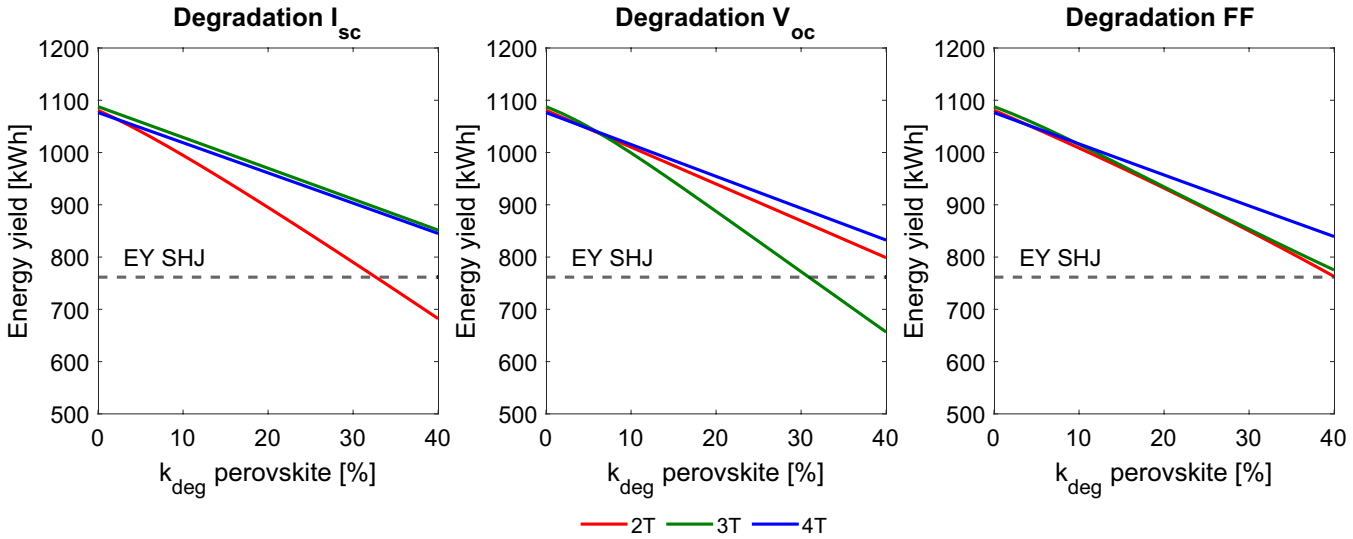

FIGURE 12 | The energy yield for all modules in Delft after different degradation scenarios. The dashed line indicates the energy yield for a single junction c-Si module.

For all scenarios, the tandem modules outperform the SHJ for values of k_{deg} up to 30%.

It should be realized, however, that the actual degradation rate of perovskite can be different for different bandgap energies. As higher bandgap perovskites tend to be less stable [53], it is possible that 3T or 4T modules reach faster high values of k_{deg} than 2T modules. This aspect should be kept in mind when comparing the degradation robustness of the different configurations.

5 | Conclusion

The perovskite/silicon technology is a promising candidate to further improve the efficiency of PV modules, that can come in different configurations. This study compares the outdoor performance of 2T, 3T, and 4T devices at the module level, considering cell-to-module losses that have not been addressed before. Using the PVMD Toolbox, the performance of a 2T PS device under outdoor conditions is validated. Then, we simulate the energy yield of each configuration across various geographical locations, identifying the optimal bandgap energies for 2T, 3T, and 4T modules of 1.62, 1.80, and 1.82 eV, respectively. Only for the 4T module there are small variations in optimal E_g across locations.

To understand the difference among the configurations, we quantify the various energy losses of all optimized modules. Additionally, the trends for all losses with respect to E_g are calculated. This shows that the differences in losses can be caused by different configuration designs (interconnection losses) or different optimal E_g (thermalization losses). The mismatch losses are the most sensitive to changes in bandgap energy, meaning they play an important role for determining the optimal E_g. Overall, all optimized configurations have similar energy yields (all differences within 1.5%) across all locations.

Finally, we quantify the degradation resilience of each configuration by simulating various degradation scenarios, being a relevant aspect to consider when comparing the configurations. Results show that 2T and 3T modules are most sensitive to current and voltage losses, respectively. Across all scenarios, the 4T configuration proves instead to be the most robust against degradation. Overall, the tandems outperform single junction modules for values of k_{deg} up to 30%.

Acknowledgments

During the preparation of this work the author used ChatGPT in order to paraphrase sentences and improve the language and readability. After using this tool/service, the author reviewed and edited the content as needed and takes full responsibility for the content of the publication.

References

1. VDMA, "International Technology Roadmap for Photovoltaics (ITRPV)," 2024.

2. 35 solar cells. 2025.

3. A. Richter, M. Hermle, and S. W. Glunz, "Reassessment of the Limiting Efficiency for Crystalline Silicon Solar Cells," *IEEE Journal of Photovoltaics* 3, no. 4 (2013): 1184–1191.

4. S. Schafer and R. Brendel, "Accurate Calculation of the Absorptance Enhances Efficiency Limit of Crystalline Silicon Solar Cells With Lambertian Light Trapping," *IEEE Journal of Photovoltaics* 8, no. 4 (2018): 1156–1158.

5. O. Er-raji, C. Messmer, A. J. Bett, et al., "Loss Analysis of Fully-Extured Perovskite Silicon Tandem Solar Cells, Characterization Methods and Simulation Toward the Practical Efficiency Potential," *Solar RRL* 7, no. 24 (2023): 2300659.

6. A. D. Vos, "Detailed Balance Limit of the Efficiency of Tandem Solar Cells," *Journal of Physics D, Applied Physics* 13, no. 5 (1980): 839–846.

7. Y. Blom, M. R. Vogt, C. M. Ruiz Tobon, R. Santbergen, M. Zeman, and O. Isabella, "Energy Loss Analysis of Two-Terminal Tandem PV

Systems Under Realistic Operating Conditions Revealing the Importance of Fill Factor Gains," *Solar RRL* 7, no. 8 (2023): 2200579.

8. "34.85%! LONGi Breaks World Record for Crystalline Silicon-Perovskite Tandem Solar Cell Efficiency Again," https://www.longi.com/en/news/silicon-perovskite-tandem-solar-cells-new-world-efficiency/, 2025. accessed on 2025-11-05.

9. K. Alberi, J. J. Berry, J. J. Cordell, et al., "A Roadmap for Tandem Photovoltaics," *Joule* 8, no. 3 (2024): 658–692.

10. S. Akhil, S. Akash, A. Pasha, et al., "Review on Perovskite Silicon Tandem Solar Cells, Status and Prospects 2T, 3T and 4T for Real World Conditions," *Materials & Design* 211 (2021): 110138.

11. Y. Shi, J. J. Berry, and F. Zhang, "Perovskite/Silicon Tandem Solar Cells," *Insights and Outlooks. ACS Energy Letters* 9, no. 3 (2024): 1305–1330.

12. E. Raza and Z. Ahmad, "Review on two-Terminal and Four-Terminal Crystalline-Silicon/Perovskite Tandem Solar Cells, Progress, Challenges, and Future Perspectives," *Energy Reports* 8 (2022): 5820–5851.

13. Y. Blom, M. R. Vogt, H. Uzu, et al., "Exploring the Potential of Perovskite/Perovskite/Silicon Triple-Junction Pv Modules in Two- and Four-Terminal Configuration," *Solar RRL* 9, no. 5 (2025): 2400613.

14. F. Fu, J. Li, T. C. J. Yang, et al., "Monolithic Perovskite-Silicon Tandem Solar Cells, From the Lab to Fab?," *Advanced Materials* 34, no. 24 (2022): 2106540.

15. X. Luo, H. Luo, H. Li, et al., "Efficient Perovskite/Silicon Tandem Solar Cells on Industrially Compatible Textured Silicon," *Advanced Materials* 35, no. 9 (2023): 2207883.

16. R. Santbergen, H. Uzu, K. Yamamoto, and M. Zeman, "Optimization of Three-Terminal Perovskite/Silicon Tandem Solar Cells," *IEEE Journal of Photovoltaics* 9, no. 2 (2019): 446–451.

17. E. L. Warren, W. E. McMahon, M. Rienäcker, et al., "A Taxonomy for Three-Terminal Tandem Solar Cells," *ACS Energy Letters* 5, no. 4 (2020): 1233–1242.

18. G. Giliberti, F. Di Giacomo, and F. Cappelluti, "Three Terminal Perovskite/Silicon Solar Cell With Bipolar Transistor Architecture," *Energies* 15, no. 21 (2022): 8146.

19. H. Schulte-Huxel, R. Witteck, S. Blankemeyer, and M. Köntges, "Optimal Interconnection of Three-Terminal Tandem Solar Cells," *Progress in Photovoltaics, Research and Applications* 31, no. 12 (2023): 1350–1359.

20. M. Hull, J. Rousset, V. S. Nguyen, P. P. Grand, and L. Oberbeck, "Prospective Techno-Economic Analysis of 4T and 2T Perovskite on Silicon Tandem Photovoltaic Modules at GW-Scale Production," *Solar RRL* 7, no. 23 (2023): 2300503.

21. Y. Zhao, R Santberge, D Zhang, et al., "Optical Design Strategies for High-Efficiency Monofacial and Bifacial Four-Terminal Perovskite-Silicon Tandem Modules," In, 2023.

22. J. Qian, M. Ernst, N. Wu, and A. Blakers, "Impact of Perovskite Solar Cell Degradation on the Lifetime Energy Yield and Economic Viability of Perovskite/Silicon Tandem Modules," *Sustainable Energy & Fuels* 3, no. 6 (2019): 1439–1447.

23. M. H. Futscher and B. Ehrler, "Efficiency Limit of Perovskite/Si Tandem Solar Cells," *ACS Energy Letters* 1, no. 4 (2016): 863–868.

24. F. Gota, M. Langenhorst, R. Schmager, J. Lehr, and U. W. Paetzold, "Energy Yield Advantages of Three-Terminal Perovskite-Silicon Tandem Photovoltaics," *Joule* 4, no. 11 (2020): 2387–2403.

25. W. E. McMahon, J. F. Geisz, J. Buencuerpo, and E. L. Warren, "A Framework for Comparing the Energy Production of Photovoltaic Modules Using 2-, 3-, and 4-Terminal Tandem Cells," *Sustainable Energy & Fuels* 7, no. 2 (2023): 461–470.

26. M. Singh, R. Santbergen, I. Syifai, A. Weeber, M. Zeman, and O. Isabella, "Comparing Optical Performance of a Wide Range of Perovskite/Silicon Tandem Architectures Under Real-World Conditions," *Nano* 10, no. 8 (2020): 2043–2057.

27. M. Kikelj, L. L. Senaud, J. Geissbühler, et al., "Do All Good Things Really Come in Threes? The True Potential of 3-Terminal Perovskite-Silicon Tandem Solar Cell Strings," *Joule* 8, no. 3 (2024): 852–871.

28. M. Vogt, C. R. Tobon, A. Alcañiz, et al., "Introducing a Comprehensive Physics-Based Modelling Framework for Tandem and Other PV Systems," *Solar Energy Materials and Solar Cells* 247 (2022): 111944.

29. Y. Blom, M. R. Vogt, O. Isabella, and R. Santbergen, "Optimization of the Perovskite Cell in a Bifacial Two-Terminal Perovskite/Silicon Tandem Module," *Solar Energy Materials and Solar Cells* 282 (2025): 113431.

30. S. Mariotti, E. Köhnen, F. Scheler, et al., "Interface Engineering for High-Performance, Triple-Halide Perovskite Silicon Tandem Solar Cells," *Science* 381, no. 6653 (2023): 63–69.

31. R. Santbergen, T. Meguro, T. Suezaki, G. Koizumi, K. Yamamoto, and M. Zeman, "GenPro4 Optical Model for Solar Cell Simulation and Its Application to Multijunction Solar Cells," *IEEE Journal of Photovoltaics* 7, no. 3 (2017): 919–926.

32. R. Siegel, "Net Radiation Method for Transmission Through Partially Transparent Plates," *Solar Energy* 15, no. 3 (1973): 273–276.

33. L. A. Castriotta, M. Zendehdel, N. Yaghoobi Nia, et al., "Reducing Losses in Perovskite Large Area Solar Technology, Laser Design Optimization for Highly Efficient Modules and Minipanels," *Advanced Energy Materials* 12, no. 12 (2022): 2103420.

34. T. Arini, L. H. Lalasari, F. Firdiyono, et al., "The Effect of Deposition Times on Preparation of SnO_2, F Conductive Glass by Indonesian Local Stannic Chloride Precursors," *IOP Conference Series, Materials Science and Engineering* 541, no. 1 (2019): 012022.

35. S. M. Kim, S. J. Park, H. H. Yoon, H. W. Choi, and K. H. Kim, "Preparation of ITO and IZO Thin Films by Using Facing Target Sputtering (FTS) Method," *Journal of the Korean Physical Society* 55, no. 5(1) (2009): 1996–2001.

36. K. Sato, Y. Goto, Y. Wakayama, Y. Hayashi, K. Adachi, H. Nishimura., "Highly Textured SnO_2, F TCO films for a-Si Solar Cells," 1993.

37. A. Rehman, E. P. Van Kerschaver, E. Aydin, W. Raja, T. G. Allen, and S. De Wolf, "Electrode Metallization for Scaled Perovskite/Silicon Tandem Solar Cells, Challenges and Opportunities," *Progress in Photovoltaics, Research and Applications* 31, no. 4 (2023): 429–442.

38. R. Witteck, H. Schulte-Huxel, H. Holst, et al., "Optimizing the Solar Cell Front Side Metallization and the Cell Interconnection for High Module Power Output," *Energy Procedia* 92 (2016): 531–539.

39. M. Zeman, J. Heuvel van den, M. Kroon, et al., *Advanced Semiconductor Analysis*. tech. rep. (Delft University of Technology, 2019).

40. T. Jung, H. Song, H. Ahn, and G. Kang, "A Mathematical Model for Cell-to-Module Conversion Considering Mismatching Solar Cells and the Resistance of the Interconnection Ribbon," *Solar Energy* 103 (2014): 253–262.

41. W. McMahon, H. Schulte-Huxel, J. Buencuerpo, et al., "Homogenous Voltage-Matched Strings Using Three-Terminal Tandem Solar Cells, Fundamentals and End Losses," *IEEE Journal of Photovoltaics* 11, no. 4 (2021): 1078–1086.

42. M. V. Khenkin, K. M. Anoop, I. Visoly-Fisher, et al., "Reconsidering Figures of Merit for Performance and Stability of Perovskite Photovoltaics," *Energy & Environmental Science* 11 (2018): 739–743.

43. M. Remec, Š. Tomšič, and M. Khenkin, "From Sunrise to Sunset, Unraveling Metastability in Perovskite Solar Cells by Coupled Outdoor Testing and Energy Yield Modelling," *Advanced Energy Materials* 14, no. 29 (2024): 2304452.

44. C. Zhao, B. Chen, X. Qiao, L. Luan, K. Lu, and B. Hu, "Revealing Underlying Processes Involved in Light Soaking Effects and Hysteresis Phenomena in Perovskite Solar Cells," *Advanced Energy Materials* 5, no. 14 (2015): 1500279.

45. S. Orooji and U. W. Paetzold, "Energy Yield Modeling of Perovskite Silicon Tandem Photovoltaics, Degradation and Total Lifetime Energy Yield," *Energy Technology* 12, no. 11 (2024): 2400998.

46. Y. Blom, M. Ruben Vogt, O. Isabella, and R. Santbergen, "Method for Bandgap Interpolation of Perovskites Spectral Complex Refractive Index," *Optics Express* 32, no. 3 (2024): 4365.

47. Y. Blom, "YBlom1999/InterpolationNK-YB, Final," 2024.

48. S. Manzoor, J. Häusele, K. A. Bush, et al., "Optical Modeling of Wide-Bandgap Perovskite and Perovskite/Silicon Tandem Solar Cells Using Complex Refractive Indices for Arbitrary-Bandgap Perovskite Absorbers," *Optics Express* 26, no. 21 (2018): 27441.

49. M. Kottek, J. Grieser, C. Beck, B. Rudolf, and F. Rubel, "World Map of the Köppen-Geiger Climate Classification Updated," *Meteorologische Zeitschrif* 15, no. 3 (2006): 259–263.

50. J. Ascencio-Vásquez, K. Brecl, and M. Topič, "Methodology of Köppen-Geiger-Photovoltaic Climate Classification and Implications to Worldwide Mapping of PV System Performance," *Solar Energy* 191 (2019): 672–685.

51. F. J. T. de las Heras, O. Isabella, M. R. Vogt, "A Machine Learning Approach to PV-A Machine Learning Approach to PV," 2024.

52. J. Remund, S. Müller, M. Schmutz, P. Graf. "Meteonorm Version 7.2," METEOTEST (www. meteotest. com), 2020.

53. K. Hossain, S. Nayak, and D. Kabra, "Challenges and Opportunities in High Efficiency Scalable and Stable Perovskite Solar Cells," *Applied Physics Letters* 125, no. 17 (2024): 170501.

Supporting Information

Additional supporting information can be found online in the Supporting Information section. Comparison_2T_3T_4T_PiP_Supporting_Information.pdf. Optimal_STC.csv. Optimal_EY_Shanghai.csv. Optimal_EY_Lisbon.csv. Optimal_EY_Lagos.csv. Optimal_EY_Delft.csv. Losses_4T_Delft.csv. Losses_3T_Delft.csv. Losses_2T_Delft.csv.